

<https://doi.org/10.1038/s44334-025-00022-3>

# Localised control of phase formation in a high-carbon low alloy steel by laser powder bed fusion



Karl Peter Davidson<sup>1,2,3</sup>, Tan Phuc Le<sup>1,4</sup>, Linh Lan Nguyen<sup>2</sup>, Jude Emil Pascua Fronda<sup>1</sup>, Ruiliang Liu<sup>5</sup>, Tzee Lui Meng<sup>6</sup>, Yee Yan Tay<sup>7</sup> & Matteo Seita<sup>4</sup>✉

The ability of additive manufacturing processes to control solidification at a microscopic scale is of particular interest in the development of components with topology-optimised microstructures. Leveraging laser powder bed fusion (L-PBF), we present a new methodology to develop site-specific “microstructure architectures” consisting of dissimilar phases. By controlling the laser focal offset in a bespoke L-PBF machine, we tailor the melt pool shape and control the volume of material that undergoes re-heating during each melting event. Using a high-carbon low alloy steel as a case study material, we demonstrate control over the formation of tempered and un-tempered phases at the resolution of the laser spot size ( $\sim 10^2 \mu\text{m}$ ) and in 3-D throughout the build. Although the tensile strength of the steel is limited by the presence of keyhole porosity and solidification cracking, our strategy showcases the opportunity to vary hardness site-specifically and by up to 2.4 GPa, opening the path to producing alloys with novel microstructure and property complexity.

The increased adoption of laser additive manufacturing by the materials science community has stimulated the research of novel processing strategies to manipulate the microstructure of metals and metal alloys and produce materials with complex, heterogeneous microstructures<sup>1,2</sup>. The main motivation behind this effort is that microstructure complexity in metals yields improved mechanical performance. This is exemplified in many classes of materials produced using conventional manufacturing processes, such as structural alloys with precipitation-hardened or duplex microstructures<sup>3,4</sup>, small-scale materials with gradient grain structures<sup>5</sup>, and other more exotic multi-material systems<sup>6</sup>.

The most common laser additive manufacturing strategies used to engineer this complexity into the microstructure of materials rely on tuning the laser parameters and laser scanning strategies site-specifically throughout the build. This has a direct effect on the local thermal history experienced by the material, which drives different solidification microstructures. Several pioneering studies demonstrated how this new manufacturing paradigm could lead to microstructures with site-specific grain size<sup>7</sup>, crystallographic textures<sup>8</sup>, and even grain boundary character distributions<sup>9</sup>. More recently, a growing body of literature has focused on the

possibility of controlling the crystallographic phases which the material solidifies into—and which it retains—throughout the additive manufacturing process. Compared to grain structure, grain orientation, and grain boundary control, in fact, “architecting” microstructural phases offers an even greater potential to enhance materials properties.

Kurnsteiner et al., for instance, succeeded in producing a multi-phase steel alloy with remarkable strength and ductility by combining precipitation-hardened and austenitic microstructures. Their strategy relied on a layer-wise control of the intrinsic heat treatment experienced by the material, which, in turn, affects the sample base temperature upon directed energy deposition (DED)<sup>10</sup>. While DED is a promising additive manufacturing technique to produce heterogeneous microstructures—especially on a large scale—its low spatial resolution and the fixed heat conduction path through the built plate limit the degree of microstructure complexity attainable. By contrast, powder bed fusion techniques such as laser powder bed fusion (L-PBF) offer finer control over heat input as well as a higher degree of freedom to engineer the heat conduction path through the use of intricate laser scan strategies as well as the strategic design of support structures. Leveraging on these

<sup>1</sup>School of Mechanical and Aerospace Engineering, Nanyang Technological University, Singapore, Singapore. <sup>2</sup>School of Materials Science and Engineering, Nanyang Technological University, Singapore, Singapore. <sup>3</sup>Photon Forge Additive Manufacturing Facility, John de Laeter Centre (JdLC), Curtin University, Perth, WA, Australia. <sup>4</sup>Department of Engineering, University of Cambridge, Cambridge, UK. <sup>5</sup>Curtin Corrosion Centre, Western Australia School of Mines, Faculty of Science and Engineering, Curtin University, Perth, WA, Australia. <sup>6</sup>Institute of Materials Research and Engineering, A\*STAR (Agency for Science, Technology and Research), Singapore, Singapore. <sup>7</sup>Facility of Analysis, Characterisation, Testing and Simulation (FACTS), Nanyang Technological University, Singapore, Singapore. ✉e-mail: [ms2932@cam.ac.uk](mailto:ms2932@cam.ac.uk)

advantages, Arabi Hashemi et al. produced duplex stainless steel with controlled distribution of the ferrite and austenite phases, both along the build direction as well as within the build plane<sup>11</sup>. Their strategy involved a variable energy density to selectively evaporate nitrogen (an austenite phase stabilizer). Using a different approach, Chen et al. demonstrated layer-wise phase control in Ti-6Al-4V by reheating the previously solidified layer with a lower energy laser scan strategy<sup>12</sup>. The reheating transformed the top portion of the  $\alpha'$  martensitic layer into an  $\alpha + \beta$  microstructure band. Although limited to layered microstructure designs, The resulting material exhibited improved elongation up to 9%. Xu et al. applied a different approach to induce the same phase transformation throughout the entire volume of Ti-6Al-4V builds by varying the laser beam focus<sup>13</sup>. They showed that by controlling the laser beam focus, which acts upon the depth of the keyhole melt pools and powder layer thickness, they could tailor the size of the heat-affected zone across subsequent layers to transform acicular  $\alpha'$  martensite into a fine  $\alpha + \beta$  lamellar structure. The resulting builds, although monolithic, exhibited yield strength in excess of 1100 MPa at elongations up to 11.4%.

Building on these prior works, we present a method to engineer the phase content of a high carbon, low alloy steel site specifically and in 3-D (i.e., both along the build direction and within the build plane). Unlike previous works, we use a fully open, in-house developed L-PBF machine that allows tuning laser parameters, and notably laser focus, in individual scan lines. This feature allows manipulating the phase content in the microstructure at the level of a single melt pool—which has never been achieved before. By alternating in-focus and defocused laser scan lines, we produce complex “microstructure architectures” of martensitic steel in 3-D. The improved microstructure design freedom offered by our strategy could be translated to commercial L-PBF systems and thus could open the path to producing alloys with novel microstructure complexity at the scale of a melt pool ( $\sim 10^3 \mu\text{m}$ ), which may offer greater opportunities in enhancing mechanical performance.

## Results

### Phase control strategy

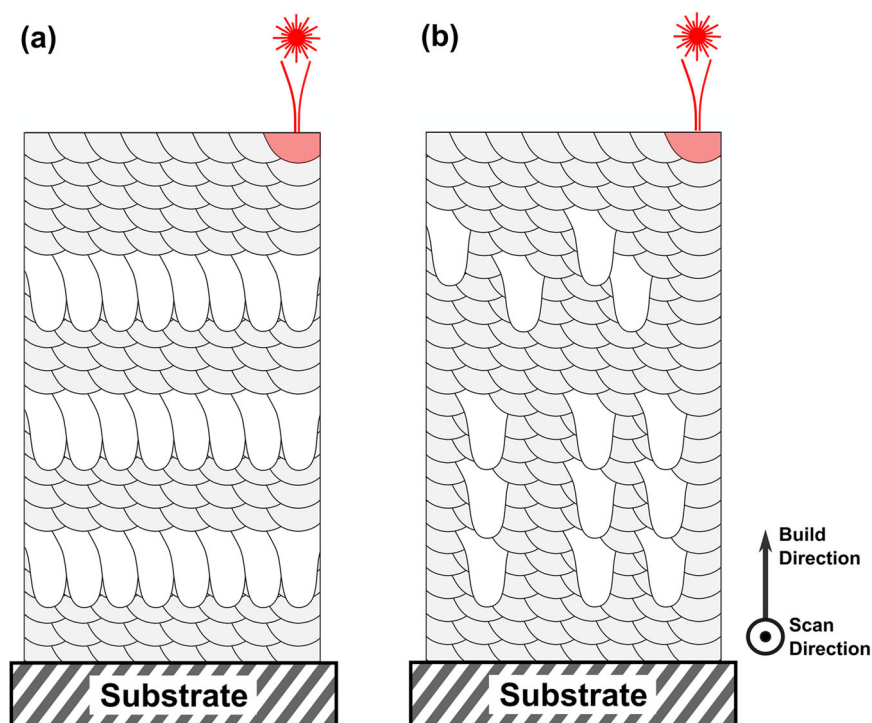
Our strategy is based on L-PBF of the alloy in conduction mode and on using keyhole mode site-specifically to change the local phase. The shallow

conduction-mode melt pools ensure a consistent intrinsic heat treatment of the underlying material, which is uniformly tempered. When switching to keyhole mode, however, the deep penetration depth of the melt pool allows remelting the material over 9 layers below, forming a metastable microstructure that is beyond reach from the intrinsic heat treatments caused by subsequent conduction-mode melt pools. As a result, the deeper portion of the keyhole melt pool retains the initial “un-tempered” metastable phase, while the top undergoes an intrinsic “tempering” step (Fig. 1). The un-tempered phases in the alloy used in this work include  $\alpha'$ -martensite and  $\gamma$ -austenite, while the equilibrated phase is expected to be  $\alpha$ -ferrite. Leveraging on the open-source nature of our L-PBF machine, we explore the possibility of controlling the alternation between these two microstructures both along the build direction (i.e., stacking melt pools of the same type horizontally) as well as within the build plane (i.e., stacking melt pools of the same kind vertically). This strategy provides us with the opportunity to design “microstructure architectures” with controlled distribution of the constituent crystallographic phases, as we show schematically in Fig. 1 and demonstrate in Fig. 2. In the latter, the two microstructures appear with stark optical contrast because of their different susceptibility to chemical etching.

To switch between keyhole and conduction mode melt pools, we vary the laser fluence, which is a function of laser spot size and intensity distribution<sup>14</sup>. One way to tune both features at once is to vary the focal offset of a pulsed laser beam. According to the laser manufacturer, each laser pulse is characterized by a peak intensity of 1100 W across an area of  $\sim 1.6 \text{ mm}^2$  when the laser is in focus (corresponding to a laser spot diameter of  $45 \mu\text{m}$ ). Under these conditions, the melt pool of the high carbon steel is in keyhole regime (Fig. 3). Not only the deeper portion of this melt pool is beyond reach from the intrinsic heat treatment generated by the subsequent conduction mode melt pools. It is also surrounded by material that is at a lower temperature since it has had a longer time to cool down compared to layers which are closer to the top surface<sup>15</sup>. As a result, this region retains the un-tempered, martensitic phase throughout the build<sup>10,16</sup>.

Moving the laser further from the focal plane spreads the peak intensity over a larger area through an increase in the beam diameter (Fig. 3)<sup>14</sup>. We compute the increase in beam diameter as a function of the decreasing distance,  $z$ , between the powder layer and the nominal focal plane of the laser

**Fig. 1 | Schematics of different microstructure architectures with different phases and melt pool geometries.** Keyhole melt pools appear in white and conduction melt pools in grey. **a** Continuous “melt pool bands” of alternating phases. **b** Vertically stacked melt pools (i.e., vertical “melt pool bands”).



using the following equation<sup>17,18</sup>:

$$d(z) = d_0 \sqrt{1 + \left(\frac{z}{0.5 \cdot \text{DOF}}\right)^2} \quad (1.0)$$

Here,  $d_0$  is the focused beam diameter (45  $\mu\text{m}$ ), and  $\text{DOF}$  is the depth of field as calculated by Eqn 2.0.

$$\text{DOF} = \frac{2\pi \cdot (0.5 \cdot d_0)^2}{\lambda \cdot M^2} \quad (2.0)$$

Here,  $\lambda$  is the laser wavelength (1064 nm), and  $M^2$  is the laser beam quality (1.3) as provided by the laser manufacturer. Given that  $z$  varies within the range of 1, 2, 3, and 4 mm above the focal plane, the corresponding laser beam diameter increases to 60, 90, 126, and 162  $\mu\text{m}$ , respectively, as shown in Fig. 3b. As a result, the more defocused the laser, the wider and shallower the melt pool (Fig. 3).



**Fig. 2** | Cross-sectional optical micrograph of an architected sample containing un-tempered  $\alpha'$ -martensite (white) consolidated in a configuration which produces the acronym “NTU”.

These differences affect the energy density,  $E$ , which is used to melt the material. Because of the large variations in melt pool geometry (depth and width) when changing laser focus offset, we shall not estimate changes in  $E$  using the conventional volumetric energy density expression,  $E = P/v \cdot h \cdot t$  (which considers a constant volume of molten material per unit time,  $v \cdot h \cdot t$ , and is independent of melt pool shape). Instead, we use<sup>19</sup>:

$$E = \frac{4 \cdot P}{\pi \cdot v \cdot d(z)^2} \quad (3.0)$$

Here,  $P$  is the laser power (200 W),  $v$  is the laser scanning speed (400 mm/s) and  $d(z)$  is the same quantity as in Eqn 1.0. Thus, for the given  $z$  of 0, 1, 2, 3, and 4 mm, we calculate a corresponding energy density of 314, 203, 79, 40, and 24  $\text{J}/\text{mm}^3$ , respectively.

To pinpoint the transition between conduction and keyhole mode in our steel alloy, we analyse a matrix of samples produced at different laser focal offsets as shown in Fig. 3b. In Fig. 4a, we plot both the depth of melt pools at the top layer as well as the bulk density of the sample. While melt pool depth decreases linearly with the level of defocus, the sample density suddenly increases beyond a defocus level of +2 mm. We associate this steep increase in density with the keyhole-to-conduction mode transition and the corresponding reduction in keyhole porosity as evidenced in the porosity figures for monolithic samples produced at each defocus level considered (Fig. 4c)<sup>14</sup>. By plotting sample density versus energy density ( $E$ ), we observe a considerable decrease in sample density for  $E > 78.6 \text{ J}/\text{mm}^3$ , and a high sample density window between  $24.3 \text{ J}/\text{mm}^3 < E < 78.6 \text{ J}/\text{mm}^3$  (Fig. 4b). When comparing average melt pool width/hatch spacing to density, as summarised in Fig. 4b, we observe an increase in density at overlaps of  $>1.25$ . This plot shows that even at the highest focus—corresponding to the narrowest melt pool width (Fig. 3a)—we maintain melt pool overlap and that the decrease in density comes from keyhole pore formation (as opposed to lack of fusion). An additional piece of evidence supporting this conclusion is in the defect maps (Fig. 4c). Here, we see a periodicity of keyhole pore formation in samples produced at 0 mm and 1 mm focal offsets, which stems from the colinear melt pools. Notable from Figs. 3b and 4a is also that the melt pool depth of a focused beam (0 mm) in keyhole regime is  $>9$  times deeper than the recoated powder layer (50  $\mu\text{m}$ ). By contrast, the greatest

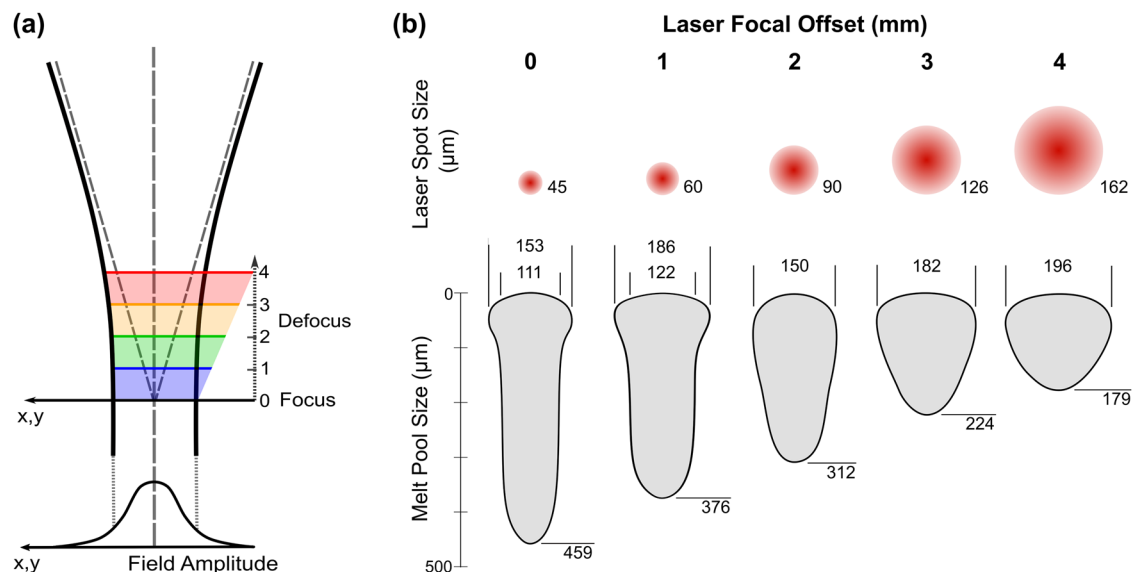


**Fig. 3** | Laser defocussing effects. Schematics illustrating the effect of laser focal offset on **a** calculated laser spot size and **b** average melt pool cross-section geometries as measured from experiments.

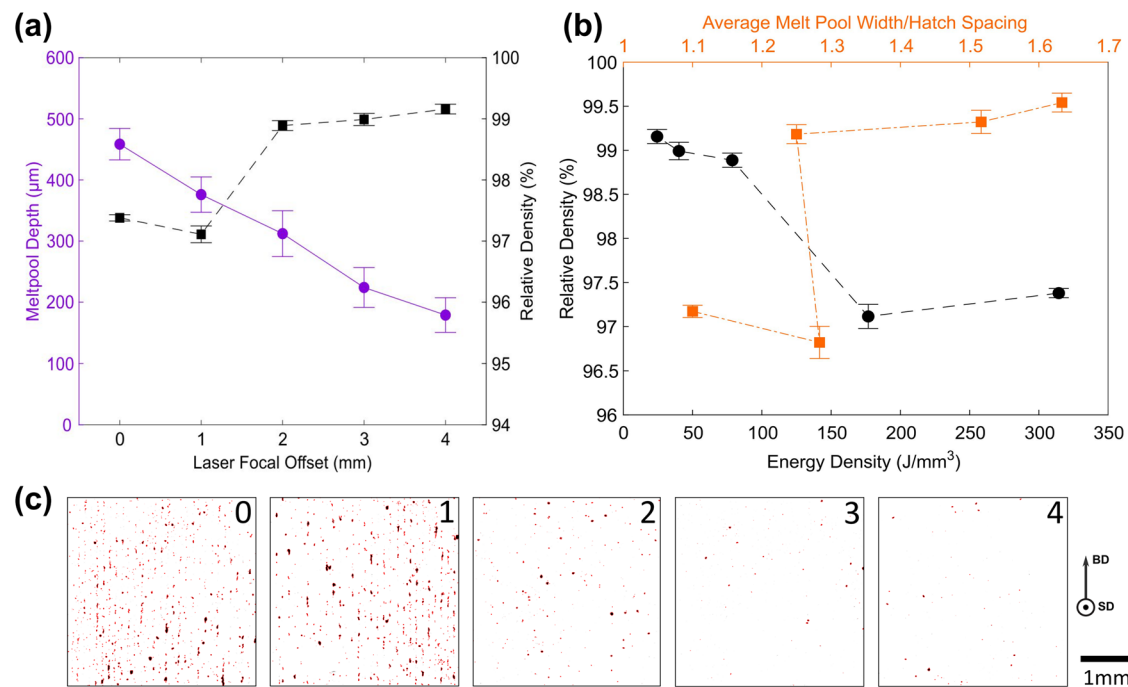


**Fig. 4 | Melt pool depth and porosity analysis.** **a** Melt pool depth and sample density with respect to laser defocus. **b** Sample density versus energy density and hatch spacing/spot size. **c** Defect maps based on optical micrographs of monolithic samples produced at each focal offset; 0, 1, 2, 3, and 4 mm (red circles denote defects).

defocus level tested (+4 mm) produces a melt pool <4 times deeper than the powder layer. Defocus levels greater than +4 mm resulted in incomplete melt pool coalescence between layers and the onset of lack of fusion porosity as presented in Supplementary Fig. 1.

The above analysis implies that the lateral resolution of our strategy is effectively limited by the focus offset itself since it changes melt pool width (between ~110  $\mu\text{m}$  and ~190  $\mu\text{m}$ , as seen in Fig. 3b). The resolution along the build direction, instead, depends on the relative difference in melt pool depth, which is largest (i.e., ~330  $\mu\text{m}$  deep) when overlapping a 4 mm defocus scan line (~180  $\mu\text{m}$  deep melt pool) atop an in-focus one (~460  $\mu\text{m}$  deep melt pool).

### Microstructure evaluation

Figure 5 shows the X-ray diffraction (XRD) analysis of the powder used and of a “banded sample” produced by alternating a layer melted using a focused laser (0 mm) every 10 layers produced using a defocused laser (+4 mm). This sample is an example of horizontal architecture (Fig. 1a). A mixture of  $\alpha$ -ferrite and  $\alpha'$ -martensite dominates the banded sample microstructure as evinced by the peaks at 44.6°, 64.9°, and 82.2°. The fact that these peaks overlap is widely reported in the literature and is due to the two phases sharing similar crystal structures with minimum differences in lattice spacing<sup>20</sup>. The inset figure focuses on the  $2\theta$  range between 43 and 46° and highlights the asymmetric  $\alpha$ -ferrite/ $\alpha'$ -martensite peak at 44.6°, which stems from the strained lattice of  $\alpha'$ -martensite and thus confirms the co-existence of both phases in the build<sup>21</sup>. The peaks at 50.5° and 43.6° stem from the retained  $\gamma$ -austenite and the presence of  $\text{Fe}_3\text{C}$  carbides, respectively. Additionally, we note that samples may contain  $\text{Fe}_7\text{C}_3$  carbides too, which produce peaks that overlap with the  $\gamma$ -austenite at 50.5° and the  $\alpha$ -ferrite/ $\alpha'$ -martensite at 82.2°, respectively. Both  $\text{Fe}_7\text{C}_3$  and  $\text{Fe}_3\text{C}$  are commonly reported in laser-based additive-manufactured steels, as they form along the carbon-enriched boundaries of  $\alpha'$ -martensite grains<sup>22–24</sup>. To distinguish between these two types of carbides in our samples we rely on EBSD<sup>25,26</sup> and TEM, as we discuss at more length hereafter. We note that all spectral peaks are aligned with those found in comparable steels produced by L-PBF, verifying their authenticity<sup>27–30</sup>.

Scanning electron micrographs and EBSD maps of a keyhole “melt pool band” (MPB) are presented in Fig. 6. Herein, we denote an MPB as a

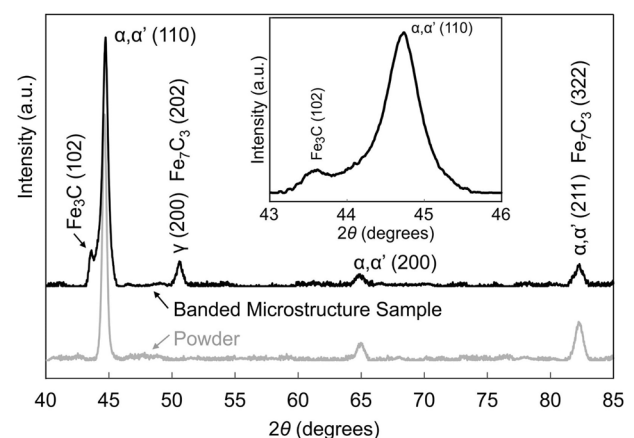
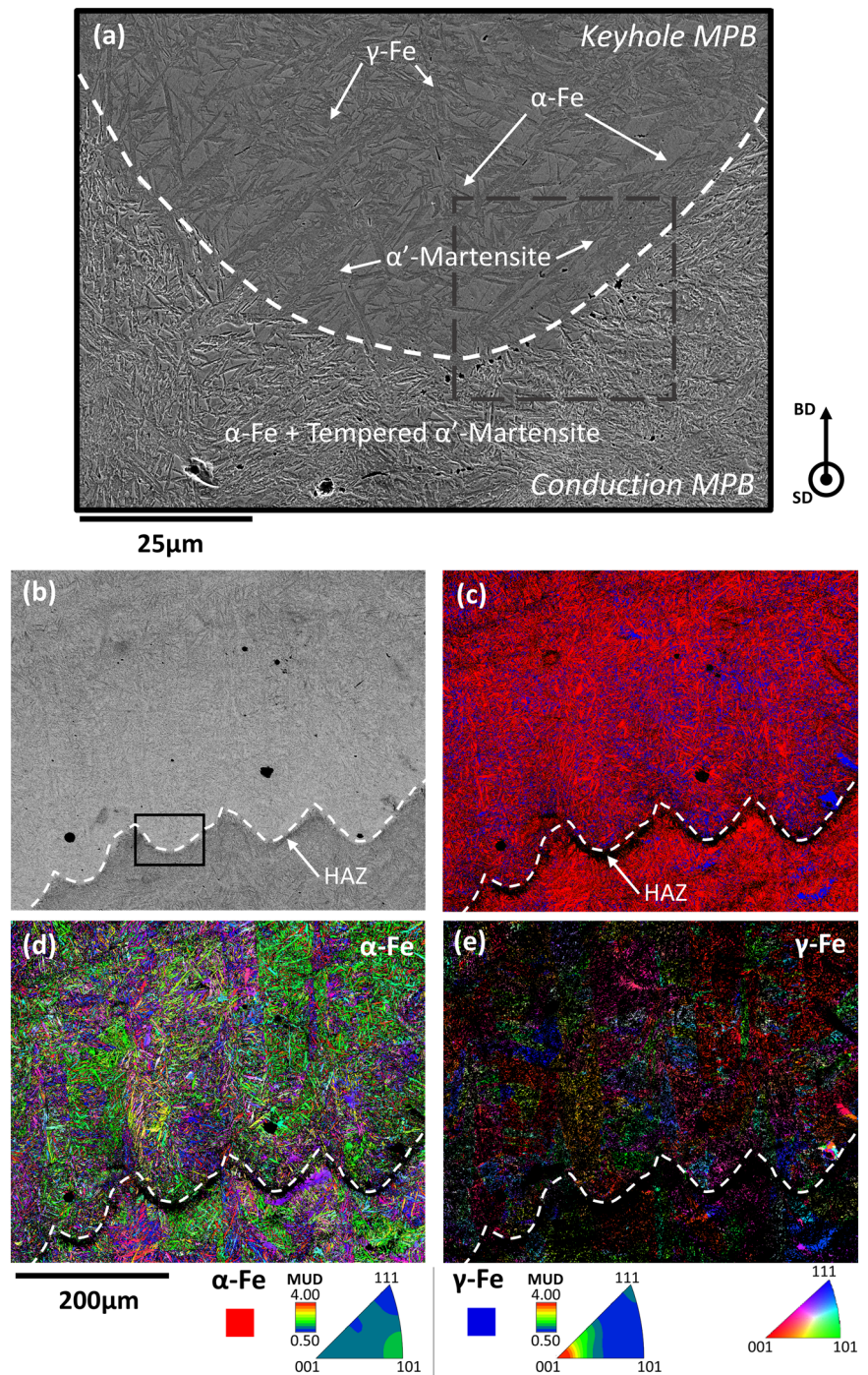


**Fig. 5 | XRD analysis of samples with different MPBs.** XRD of banded microstructure sample produced with our L-PBF strategy. Inset denotes peaks between 43 and 46° of banded microstructure sample. The powder XRD spectrum provides a baseline measurement.

portion in the build consisting of melt pools produced using constant laser focus, either in the keyhole or in conduction mode, which extends laterally across the entire area of the layer. MPBs may have different thickness depending on how many layers have been melted using the same melting mode. When using keyhole mode, the MPB will exhibit a metastable microstructure. By contrast, when using conduction-mode melting, the MPB will consist of a more normalised microstructure. Noteworthy is that an MPB differs from the “fusion zone” region which is often described in welding and additive manufacturing literature, as it encompasses the entire volume of all adjacent melt pools produced using the same focus level, which thus have the same microstructure (as depicted by the white melt pools in Fig. 1). The fusion zone of a MPB divides such a volume from that of other melt pools or MPBs of different nature. At the scale of an individual keyhole melt pool (Fig. 6a), we observe a clear contrast between the region below the melt pool boundary line, which has been tempered by the intrinsic heat treatment, and the un-tempered melt pool itself. The difference in contrast



**Fig. 6 | EBSD maps of MPBs.** **a** Microstructure of a keyhole MPB sandwiched in between tempered conduction MPBs. The grey dashed boundary denotes a region observed in high magnification EBSD of Fig. 7, **b** Microstructures of a MPB dominated by  $\alpha'$ -martensite (etched sample with square presented in **a**) and corresponding SEM image, **c** phase map, **d** out-of-plane grain orientation map for  $\alpha$ -Fe and, **e** out-of-plane grain orientation map for  $\gamma$ -Fe with corresponding inverse pole figures for both phases (step size 0.15  $\mu\text{m}$ ). The dashed white line denotes the melt pool boundary with HAZ directly below the line.



in these micrographs is opposite to that found in Fig. 2, where the melt pool tips appear light under the optical microscope. Similar optical contrast was reported in L-PBF of carbon steels by Dilip et al. and Hearn et al., where the un-tempered  $\alpha'$ -martensite was characterized by light regions owing to their smoother surface and higher reflectivity compared to the preferentially etched tempered regions<sup>22,31</sup>. The reason why the contrast is reversed in electron micrographs is that a corrugated surface (i.e., that of tempered regions) scatters more secondary electrons compared to a smooth surface (i.e., that of the un-tempered regions). Following this rationale, we conclude that melt pool tips have higher  $\alpha'$ -martensite content compared to the tempered regions, due to the higher corrosion resistance of this phase compared to  $\alpha$ -ferrite<sup>32</sup>. This conclusion is supported by an EBSD band contrast map from a similar region, which we present in Supplementary Fig. 2, as well as the hardness study, which we detail later.

To map the occurrence of different phases in different MPBs, we take the EBSD measurements shown in Fig. 6, which encompass a keyhole MPB (top) and a conduction MPB (bottom).

The two MPBs are separated by black un-indexable regions situated below the keyhole MPB boundary. This is clearly visible in Fig. 6c–e, where we outline the MPB boundary using a white dashed line, as well as in the matrix of the “NTU” sample (Fig. 2). We hypothesize that these regions in the heat-affected zone (HAZ) are over-tempered following previous reports in the literature<sup>22,24,28</sup>. These HAZ regions undergo tensile stress during cooling from the shrinkage of the melt pool, resulting in a high stress gradient and poor EBSD index quality<sup>33–35</sup>. As per the XRD results presented in the prior section, EBSD (Fig. 6c) reveals the presence of  $\alpha$ -ferrite and  $\gamma$ -austenite in the keyhole MPB. Distinguishing between  $\alpha'$ -martensite and  $\alpha$ -ferrite is equally challenging by means of EBSD as it is by XRD (Fig. 5) owing

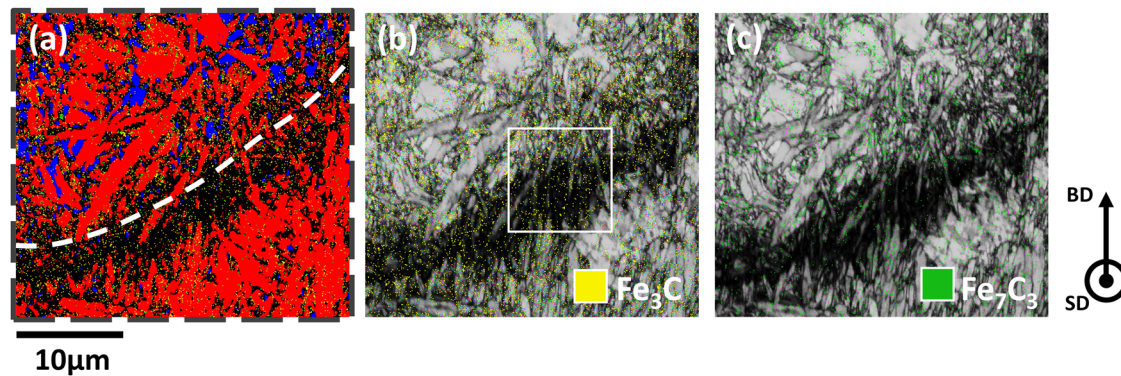


**Fig. 7 | High resolution EBSD analysis.** **a** High magnification maps (step size 0.08  $\mu\text{m}$ ) of the tip of a keyhole MPB and corresponding phase map with white dashed line denoting melt pool boundary, **b**  $\text{Fe}_3\text{C}$  phase & band contrast map and,

**c**  $\text{Fe}_7\text{C}_3$  phase & band contrast map. Grey dashed boundary denotes region taken from low magnification EBSD (Fig. 6a). White square denotes region in TEM observations Fig. 8.

**Table 1 | Melt pool phase ratio comparison**

Sample	$\alpha$ -Fe (%)	$\gamma$ -Fe (%)	$\text{Fe}_3\text{C}$ (%)	$\text{Fe}_7\text{C}_3$ (%)
Keyhole MPB	$61.3 \pm 2.2$	$29.5 \pm 2.4$	$7.5 \pm 0.3$	$1.7 \pm 0.2$
Conduction MPB	$74.5 \pm 1.9$	$15.6 \pm 0.7$	$7.8 \pm 1.1$	$2.1 \pm 0.2$

to the low degree of tetragonality of the  $\alpha'$ -martensite lattice<sup>36</sup>. However, the presence of retained  $\gamma$ -austenite here is indicative of a metastable (untempered) microstructure, which is less prominent in the conduction MPB underneath. This is even more evident in the higher-resolution EBSD imaging of a keyhole melt pool boundary, which we present in Fig. 7a–c. From this EBSD analysis, we compute a relative difference of about 10% in phase content between the two regions above and below the melt pool boundary (see Table 1). Comparable  $\gamma$ -austenite fractions were reported by Kim et al. for a L-PBF processed martensitic steel owing to supersaturation of carbon in  $\gamma$ -austenite between 0.75–1.99 wt%, evident of the quench and partitioning treatment in which carbon diffuses from the supersaturated  $\alpha'$ -martensite to  $\gamma$ -austenite in the keyhole MPB<sup>30</sup>. To validate the  $\alpha'$ -martensite and  $\alpha$ -ferrite content, we conducted Feriscope measurements on a sample with horizontal MPB architecture keyhole versus conduction MPB ratio of 1:10 (i.e., 1 keyhole melt pool layer every 10 conduction melt pool layer) reporting a ferrite content of 40.33%, which is comparable to the  $\alpha$ -ferrite ratio in the MPB measured by EBSD and presented in Table 1.

Grain size and texture analysis from the measurements in Fig. 6 provide further evidence of the tempering effect in the HAZ below the keyhole MPB. On average,  $\gamma$ -grains are measured to be  $\sim 6.7 \mu\text{m}$  in diameter, while  $\alpha'/\alpha$ -grains exhibit a slightly larger diameter of  $\sim 7.2 \mu\text{m}$  inside the keyhole MPB. In the tempered zone, grain size slightly increases with  $\gamma$ -grains and  $\alpha'/\alpha$ -grains reaching  $\sim 6.9 \mu\text{m}$  and  $\sim 8.7 \mu\text{m}$  in diameter, respectively. This difference is expected, as the keyhole MPB is least affected by the reheating induced by the subsequent layer. Our results are comparable to those reported in laser-melted martensitic steel (6.3 and  $20.1 \mu\text{m}$ )<sup>27</sup>. Overall, the alloy's crystallographic texture is weak in all phases (Fig. 6e). However, we observe the greatest texture strength in  $\gamma$ -austenite, with a  $\langle 001 \rangle$  crystallographic orientation along the build direction, which is common in steels produced by L-PBF<sup>37–39</sup>. By contrast, the  $\alpha$ -ferrite texture (Fig. 6d) is much more random, as it is often found in  $\alpha'$ -martensite-dominated steels produced by L-PBF<sup>27,28,31,40</sup>.

The high-resolution EBSD map of the melt pool tip in Fig. 7 also shows the presence of different carbides,  $\text{Fe}_3\text{C}$  and  $\text{Fe}_7\text{C}_3$ , which precipitate along  $\alpha'$ -martensite grain boundaries. This observation is in line with what Binkley reported for the same base alloy<sup>41</sup>. Preliminary analysis of relative phase fractions from these measurements indicates a preference for  $\text{Fe}_3\text{C}$  precipitation compared to  $\text{Fe}_7\text{C}_3$  in the un-tempered region (see Table 1). However, both phases are at the resolution limit for EBSD, which is why we

conducted the additional TEM measurements reported in Fig. 8. We carry out these measurements from regions in the HAZ below a keyhole MPB. The images show the presence of needle-like carbides, which we characterize to be  $\epsilon$ - $\text{Fe}_3\text{C}$  using selected area electron diffraction (SAED). We find them in clusters at a distance from one another of  $\sim 15 \text{ nm}$ , and we measure their length to be  $\sim 230 \text{ nm}$  on average (Fig. 8b, c). The formation of  $\epsilon$ - $\text{Fe}_3\text{C}$  was reported by Liu et al. to be induced by precipitation from the supersaturated  $\alpha'$ -martensite<sup>42</sup>. Additionally, we observe the formation of ellipsoidal precipitates 20–30 nm wide and 50–60 nm long (Fig. 8d). Similar precipitates were observed in the un-tempered  $\alpha'$ -martensite region of L-PBF produced steel by Hearn et al. and hypothesised to be  $\text{Fe}_3\text{C}$  carbides due to their high carbon content<sup>22</sup>.

We quantify the carbide fraction in this region through precession electron diffraction (PED), as shown in Fig. 9. The results evince a high fraction of carbides in this region of the HAZ, with low  $\alpha$ -ferrite and  $\gamma$ -austenite content due to the high diffusion of  $\text{Fe}_3\text{C}$  from tempered  $\alpha'$ -martensite. As a result, 48.4% of the PED pattern phase map (Fig. 9a) is taken up by  $\alpha'$ -martensite grains separated by  $\epsilon$ - $\text{Fe}_3\text{C}$  needles, as shown in the circled region in Fig. 9a. These results are in line with what was previously observed in laser processed carbon steel by Liu et al.<sup>42</sup>.

We interpret the above results on the basis of the intrinsic heat treatment generated by each melting event into the surrounding material. The short cooling times which result from the L-PBF process (i.e., between 0.0147 s and 0.000147 s) result in cooling rates within the range of  $10^5$ – $10^7 \text{ }^\circ\text{C/s}$ <sup>43</sup>. These cooling rates lead to supersaturation of carbon within the austenite lattice, which results in the formation of  $\alpha'$ -martensite. The occurrence of subsequent melt pools induces a HAZ which tempers this metastable microstructure to an extent that varies as a function of melt pool shape and distance from the melt pool boundary. Since the top layer of our builds (e.g., the one shown in Fig. 2) is not tempered by subsequent melting events, they all exhibit this metastable microstructure.

Deep keyhole melt pools encompass a greater volume of the underlying, prior solidified material, which extends further away from the subsequent melt pools and their HAZ. As a result, the keyhole melt pool tip consists of a metastable microstructure that includes high-temperature and metastable phases (i.e.,  $\gamma$ -austenite and  $\alpha'$ -martensite) and carbides, which precipitate in the melt pool and along the HAZ Fig. 7b, c. This microstructure is increasingly tempered along the build direction, as it approaches the HAZ induced by the melt pool on the above layer and thus experiences the intrinsic heat treatment more strongly. This results in a gradual microstructure equilibration. Upon tempering, it has been reported that the retained  $\gamma$ -austenite mostly decomposes into cementite ( $\text{Fe}_3\text{C}$ ) particles within an  $\alpha$ -ferrite matrix. This is in line with the phase ratio analysis presented in Table 1, which shows a reduction in  $\gamma$ -austenite content in the tempered region and an increase in  $\alpha$ -ferrite<sup>44–46</sup>. Noteworthy is that the



**Fig. 8 | TEM analysis of phase content.** **a**  $\alpha'$ -martensite-rich HAZ including a fast Fourier transform (FFT) image as inset, which shows the diffraction pattern of an  $\epsilon$ -Fe<sub>3</sub>C carbide needle, **b**  $\epsilon$ -Fe<sub>3</sub>C carbide needle cluster, and **c** corresponding dark field image, **d** Image of ellipsoidal precipitates.

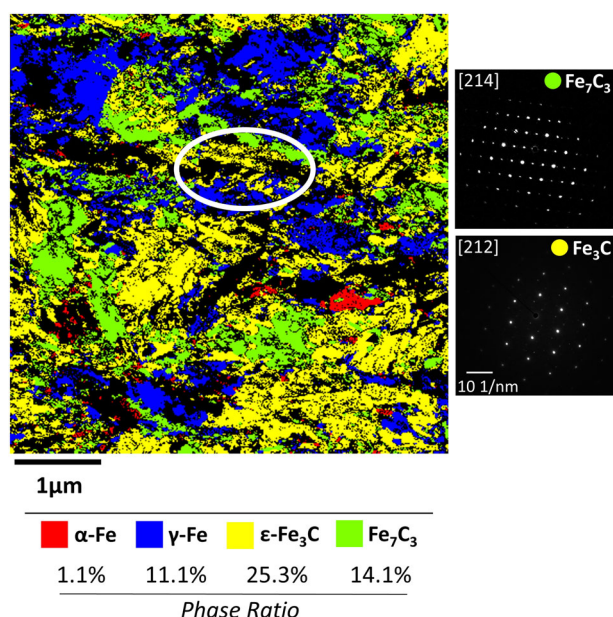
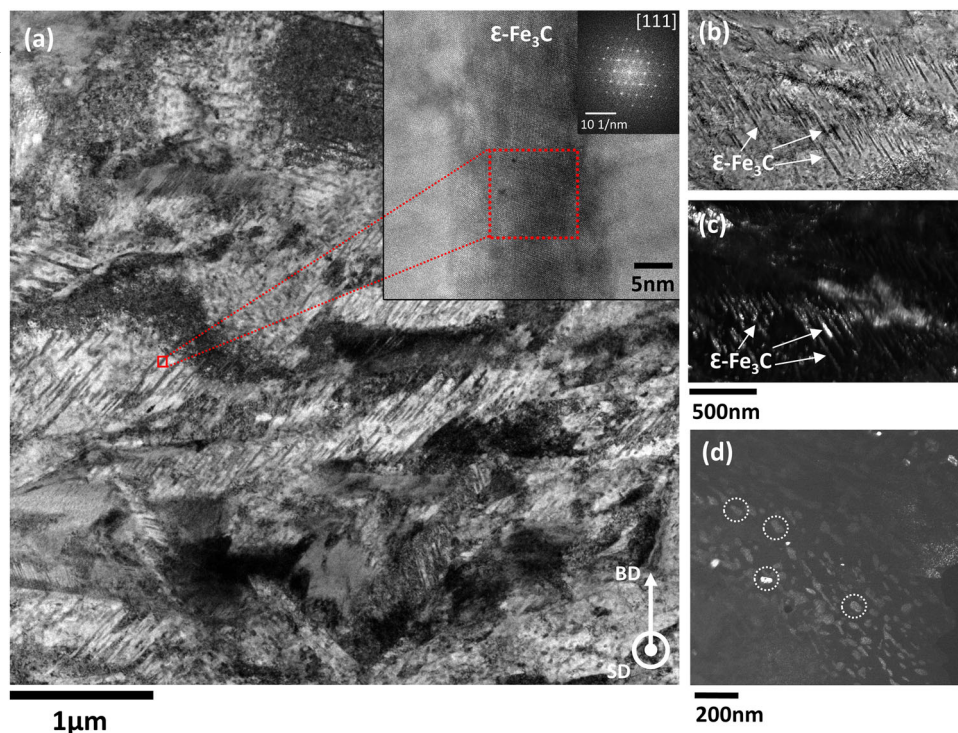


**Fig. 9 | TEM analysis of carbides.** Precession electron diffraction (PED) phase map and phase ratio with corresponding Fe<sub>3</sub>C and Fe<sub>7</sub>C<sub>3</sub> SAED patterns of the HAZ.

carbide ratio in both tempered and un-tempered zones is similar (Table 1). We interpret this result based on the different mechanisms for carbide formation in either microstructure: diffusion of Fe<sub>3</sub>C from  $\alpha'$ -martensite in the keyhole MPB region, and decomposition of  $\gamma$ -austenite in the tempered region. In contrast to the variable tempering effects found in keyhole melt pools, samples consolidated at a fixed focal offset that is conducive to conduction-mode melt pools consist of monolithic, tempered microstructures throughout, as shallower and wider conduction-mode melt pools are more easily tempered when repeated across multiple layers and undergo consistent intrinsic heat treatment.

### Nano hardness response

The MPB formation reported in the previous section imparts changes in the local mechanical properties. In Fig. 10, we present the nano-hardness of a single keyhole MPB (appearing in white) consolidated at a focal offset distance of 0 mm and sandwiched in between conduction MPBs consolidated using a defocus laser of +4 mm. The average nano-hardness change along the build direction (Fig. 10b) correlates well with changes in image contrast. The difference in hardness between tempered and un-tempered regions approaches 2.4 GPa. The rapid increase in hardness over the first 40–60  $\mu$ m from the melt pool boundary is related to the higher  $\alpha'$ -martensite content and a lower fraction of the softer  $\gamma$ -austenite<sup>22,47</sup>. We measure the highest hardness to be ~9.4 GPa at 60  $\mu$ m from the boundary. This value is comparable to what a steel alloy containing a comparable 1.2 wt% carbon with >80% volume fraction of  $\alpha'$ -martensite would exhibit<sup>48</sup>. Between 60 and 160  $\mu$ m from the boundary, hardness readings plateau at ~9.0 GPa, decreasing slightly between 180 and 260  $\mu$ m to 8.0 GPa. We ascribe this slight decrease to an increase in the retained  $\gamma$ -austenite phase (also plotted in Fig. 10b)<sup>49</sup>. Above 280  $\mu$ m from the boundary, hardness readings drop to the same levels found below the boundary as a result of the localised heat treatment and consequent microstructure tempering.

### 3-D microstructure architectures

The ability to change the melt pool shape of an individual laser scan line enables the development of complex, heterogeneous microstructures with combinations of horizontal and vertical MPBs (i.e., the two architectures shown in Fig. 1). One such example is the “NTU” sample shown in Fig. 2, where we vary the number of melt pools per MPB, and stack them either vertically or horizontally. Controlling the spacing between each of these MPBs is critical to minimise the tempering effect induced by the neighbouring MPB. In Fig. 11, we study the variation of the nano-hardness profiles along the build direction as a function of the number of layers in between horizontal keyhole MPBs when using fixed laser parameters and focus levels. We use nano-hardness measurements at 20  $\mu$ m intervals as a proxy for microstructure analysis instead of EBSD because of the higher measurement throughput attainable. We use a sample which we produced by stacking keyhole MPBs at laser focus separated by conduction MPB of 2,

**Fig. 10 | Nanohardness mapping.** **a** Optical micrograph showing nanohardness indents across different MPBs, and **b** average hardness results versus austenite fraction taken from EBSD maps.

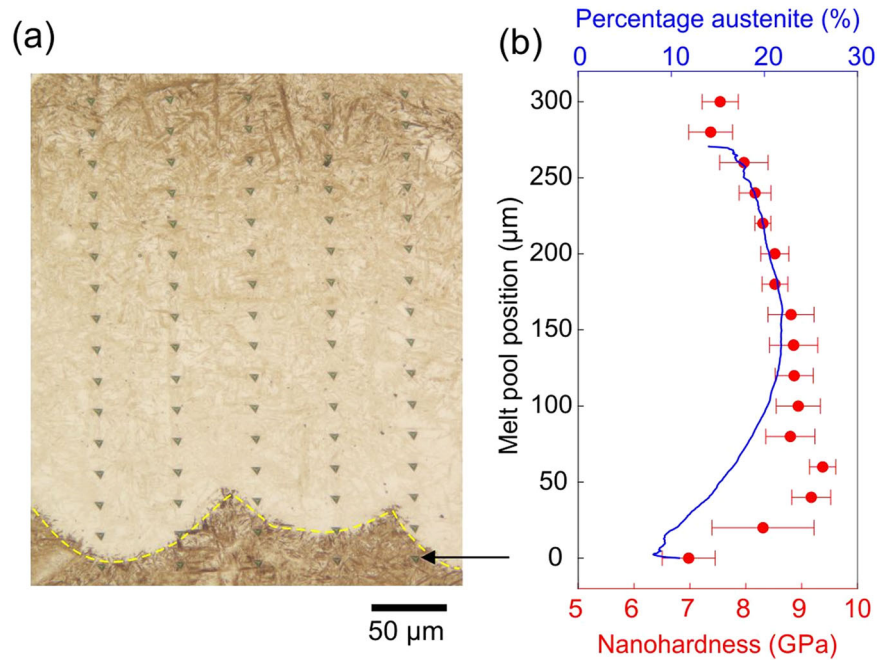
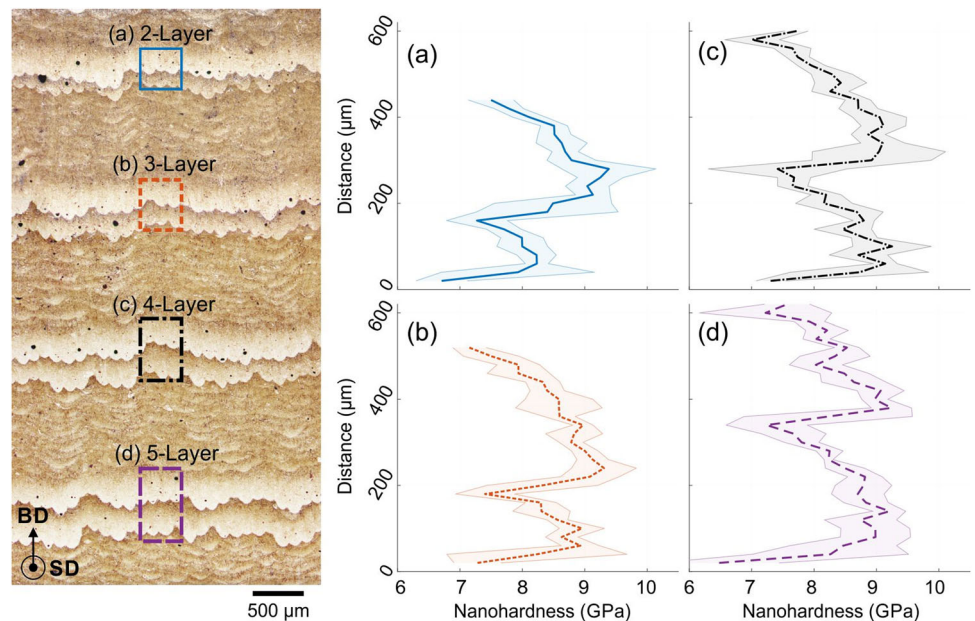


**Fig. 11 | Property contrast: Nanohardness.** **a–d** Multilayer MPB sample with varying keyhole MPB spacing: 2, 3, 4, and 5 layers, and corresponding Nanohardness results.



3, 4, and 5 layers thickness (+4 mm defocus). The etched cross-section of the sample is shown in Fig. 11a. The figure includes a control line representing the average hardness of the bulk, tempered microstructure (7.35 GPa), which we use as a reference to evaluate the hardness increase in the un-tempered regions. Given the comparable size of indents ( $\sim 6.5 \mu\text{m}$ ) and grains in the microstructure ( $\sim 10 \mu\text{m}$ ), different measurements may hit different phases and lead to significant variability in hardness. To account for that, we repeated each hardness measurement from the same region three times. In Fig. 11b we plot the measurement standard deviation as a shaded region around the mean values.

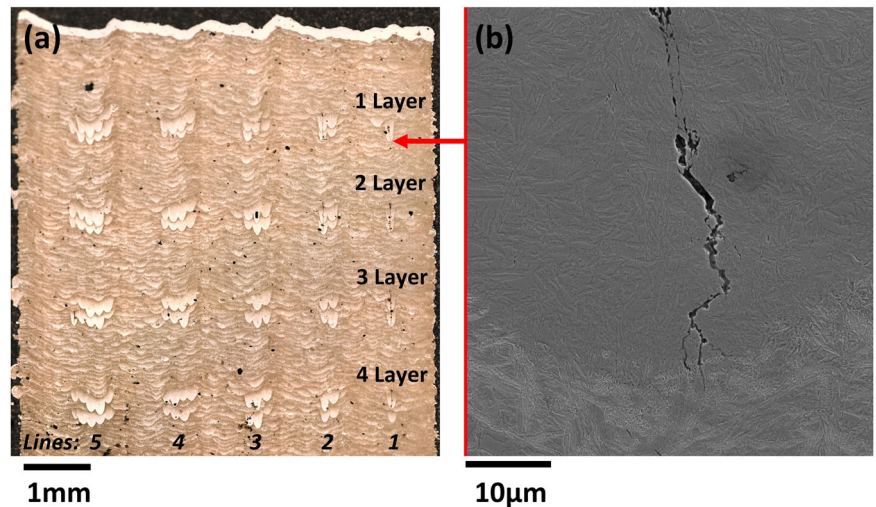
In general, hardness values increase to a maximum from the bottom keyhole MPB along the build direction, followed by a decrease to a minimum when probing the region within the conduction MPB, and finally raising again to a second maximum. The widening distance of

these two hardness peaks is evident with increasing spacing between keyhole MPBs and relates to an improvement in the definition of the microstructure architecture. Intuitively, keyhole MPBs that are too close to one another along the build direction result in excessive tempering, which is conducive to lower peak hardness in the bottom keyhole MPB and, thus, lower differences in hardness across the different MPBs. We include these two parameters in the corresponding hardness profiles. The tempering effect of the later keyhole MPB is clearly evident in regions where the two MPBs are spaced 2 and 3 layers apart (Fig. 11a, b), showing tempering of the prior solidified keyhole MPB by 1.15 GPa in the 2 layer and 0.36 GPa in the 3 layer region. At 4 and 5 layer spacings the tempering effect of the later keyhole MPB is minimal. However, the overall peak hardness values slightly increase with 5 layer spacing (Fig. 11d), which is expected due to less thermal interaction from the



**Fig. 12 | Spatial resolution of phase control.**

**a** Multilayer architected sample showing vertical MPB formation, and **b** centreline solidification cracking.



subsequent keyhole MPB. Comparable results are observed at layer spacings  $>5$ , given lesser thermal interaction between keyhole MPBs.

From the 2-layer spaced keyhole MPB results (Fig. 11a), we see local minima in hardness corresponding to the tempered region at  $140\text{ }\mu\text{m}$  from the first indentation. This distance increases to  $320\text{ }\mu\text{m}$  in the 5-layer spaced keyhole MPB region (Fig. 11d). Furthermore, the peak-to-peak distance between hardness maxima determines the resolution of each of the keyhole MPB spacing's tested. As the peak in hardness corresponds to the high volume content of un-tempered  $\alpha'$ -martensite at the bottom of the melt pool, we observe that the top keyhole MPB (later solidified) is harder than the bottom one (which is tempered by the top MPB). This results in a peak hardness reduction of  $0.378$  and  $1.154\text{ GPa}$  (Fig. 11a, b) when spacing MPBs from 3 to 2 layers respectively.

Layer spacing of 4 and 5 show a difference in peak-to-peak hardness values below  $<0.138\text{ GPa}$ , which suggests negligible tempering and retention of the metastable microstructure. We conclude that these conditions are best to retain large hardness differences and to minimize tempering when architecting different keyhole MPBs. The sample shown in Fig. 2 was produced using a 5-layer spacing.

As showcased by the “NTU” sample (Fig. 2) we also present the ability to control phases along the build direction, by stacking the same melt pool type vertically (and thus by changing from keyhole to conduction mode within the same layer). To assess the spatial resolution of our strategy along this direction, we produced an additional sample (Fig. 12) with melt pools spaced every 1–4 layers at increasing line arrangement (1, 2, 3, 4 lines) using a fixed hatch spacing of  $120\text{ }\mu\text{m}$ . The results show that the spatial resolution is down to an individual melt pool (i.e., one laser track), which is  $\sim 100\text{ }\mu\text{m}$  wide. The optical contrast suggests minimum tempering from the adjacent conduction mode melt pools, which solidify before and after the keyhole melt pool.

Noteworthy in this sample is the macroscopic waviness found at the sample surface in correspondence of MPBs, which stems from differences in the melting interaction of keyhole and conduction mode melt pools with the metal powder as well as the serpentine scan strategy used in this work<sup>50,51</sup>. Because of their different dimensions (Fig. 3b), when conduction and keyhole melt pools occur sequentially, one after the other, within the same layer, they accumulate different powder volumes<sup>52,53</sup>. This phenomenon is further exacerbated by the use of a serpentine scan strategy as well as by the local powder density during recoating, which is influenced by the peaks and troughs of the underlying solid metal<sup>54–56</sup>.

Evident in Fig. 12b is also the formation of cracks, which grow from the base of the MPBs into multiple layers. Solidification cracking is widely reported in the literature and is often associated with the grain structure in keyhole melt pools, which consists of columnar grains coalescing at the melt pool centreline. The higher solute content at this location reduces the alloy's

melting point resulting in a liquid film that cracks open under the effect of the tensile stresses induced during contraction of the surrounding solid phase as it cools<sup>57–59</sup>. Further cracking susceptibility considerations include variations in local alloy composition and phase transformations. In the case of carbon steels, the ratio between manganese and sulphur content is critical in preventing the formation of the low melting point compound FeS, which segregates along grain boundaries and increases the temperature range of solidification<sup>57</sup>. However, with carbon contents above  $0.2\text{ wt}\%$ —as is the case in this work—the effects of carbon on the cracking susceptibility and the level of un-tempered  $\alpha'$ -martensite along the melt pool boundaries is reportedly more significant<sup>60</sup>. Thus, we conclude that the centerline cracking started in the brittle, un-tempered  $\alpha'$ -martensite due to solidification shrinkage and propagated across multiple layers because of the vertical melt pool stacking resulting from the serpentine scanning strategy.

### Tensile properties of banded microstructure architectures

Using the phase-control ability that we have achieved, we produce a sample with horizontal architecture (Fig. 1a) to assess its tensile behaviour and compare it against a sample with monolithic microstructure produced using conduction mode melting. The results are shown in Fig. 13. We also report the fracture stress and strain in Table 2. The goal of this experiment was to achieve improved mechanical properties following the design proposed by Kurnsteiner et al.<sup>10</sup>. By alternating bands of hard and soft regions, in fact, it should be possible to trigger the additional hetero-deformation induced strengthening brought about by the establishment of back and forward stresses in the soft and hard regions, respectively<sup>6</sup>. Our design consisted of alternating individual keyhole MPBs with un-tempered (hard) microstructure produced using a focus laser beam and 9-layer-thick conduction MPBs of tempered microstructure produced at  $+4\text{ mm}$  focal offset.

Upon testing, we notice an overarching brittle behaviour in both samples, which is confirmed by the limited plasticity seen in the stress-strain curves as well as the characteristic morphology of the fracture surfaces (Fig. 13b–e). The coarse cleavage planes shown in Fig. 13b are representative of the homogenous microstructure in the monolithic sample, with minimal evidence of secondary cracking across the fracture surface. In the low magnification image (Fig. 13d) we can see the homogeneity of the fracture surface with sporadic lack of fusion pores induced by the shallow conduction mode melt pool. We observe similar cleavage in the architected sample albeit with more ductile dimpling (Fig. 13c), as well as with secondary, intergranular cracking, which likely formed along the melt pool length as also seen in comparable martensitic steels<sup>61,62</sup>. Observing the whole fracture surface, in Fig. 13e, we can see evidence of cleavage features following the banded horizontal architecture (white dashed lines). These cracks are likely initiated along prior  $\gamma$ -austenite grain boundaries in the un-tempered microstructure regions (Fig. 6c)<sup>63</sup>. Crack nucleation in a similar

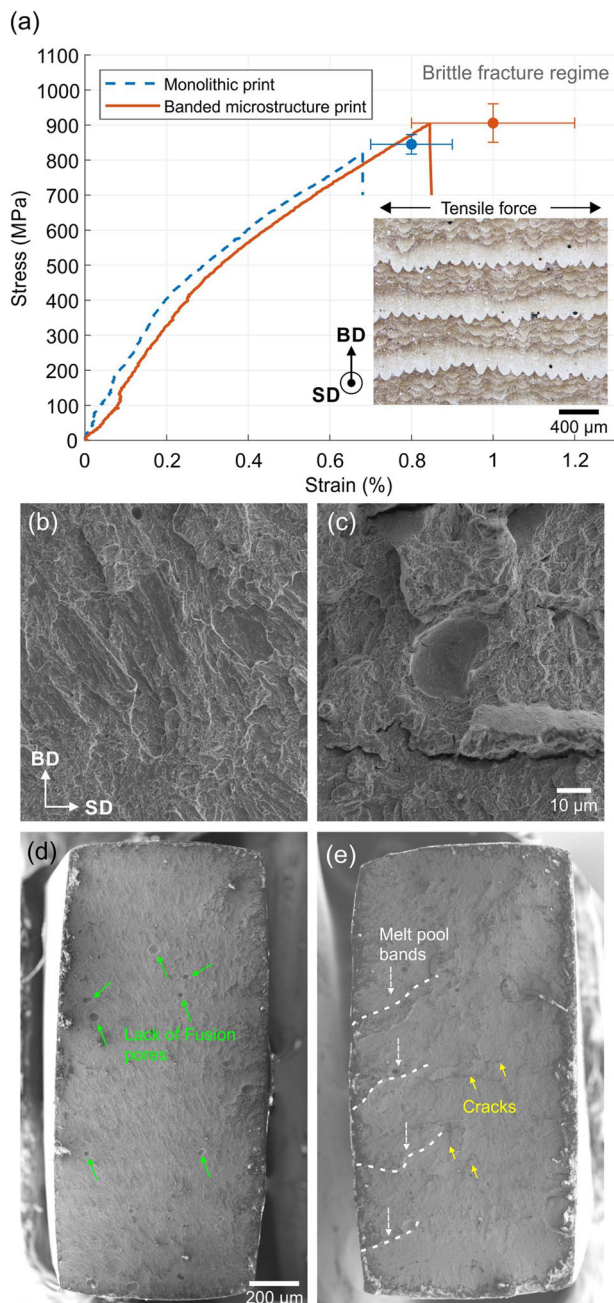


**Fig. 13 | Mechanical testing.** **a** Tensile results of banded microstructure and monolithic samples and fracture surface of, **b, d** monolithic, and **c, e** banded samples.

**Table 2 | Tensile results**

Sample	Fracture stress (MPa)	Fracture strain (%)
Banded microstructure print	905.7 ± 55.0	1.4 ± 0.7
Monolithic print	845.0 ± 28.1	0.8 ± 0.1

alloy has been reported to begin at blocky retained austenite-martensite island boundaries, resulting in trans lath fracture<sup>64</sup>. Quenched steels with carbon contents above 0.5% are reported to be susceptible to intergranular fracture and quench embrittlement after tempering at temperatures between 150 and 200 °C<sup>63</sup>. Furthermore, quench embrittlement is a function of the phosphorus content of the alloy, with high phosphorous content reducing the level of carbon addition to initiate intergranular cracking<sup>63</sup>. Considering the low phosphorus content in our alloy (0.007 wt%), however,

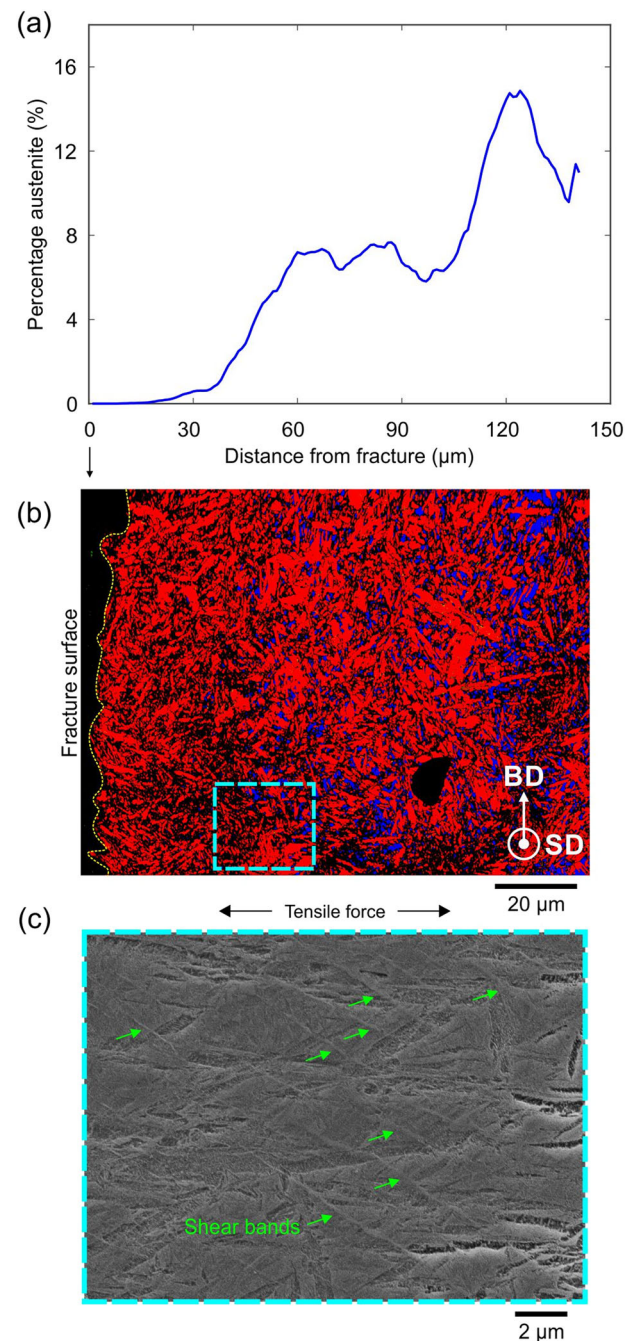


**Fig. 14 | Phase content analysis at the fracture surface.** **a**  $\gamma$ -austenite percentage from the fracture surface end, **b** EBSD phase map of the fracture surface (square represented in (c)) and **c** shear bands in the work hardened region. (step size 0.4 μm).

it is more likely that the high carbon content (1 wt%), the presence of  $\alpha'$ -martensite, and the high volume fraction of carbides ( $\text{Fe}_7\text{C}_3$  and  $\text{Fe}_3\text{C}$ ) are the main factors behind the alloy's brittleness<sup>63,65</sup>.

Aside from the brittle-like behaviour of the samples, we notice that the banded sample exhibits 100 MPa higher strength compared to the monolithic sample, reaching ~900 MPa. This evidence suggests that crack propagation is hindered when introducing controlled microstructure heterogeneities (such as different MPBs), which may have beneficial effects on the strength of the material. A more detailed investigation of these regions on the fracture surface (Fig. 14a, b) reveals an increasing gradient in  $\gamma$ -austenite content, from being absent within the first 20 μm from the surface to increasing significantly in the deeper portion away (35 μm and 60 μm) from it. This finding confirms that the region under analysis is



indeed characterized by the un-tempered microstructure due to the increased retained  $\gamma$ -austenite content, which is similar to that seen in the keyhole MPB of Fig. 6c. It also suggests that the strength increase measured in the banded sample is due to its higher retained austenite content—rather than to hetero-deformation induced strengthening—which is likely to work harden and transform into martensite upon increasing load<sup>49,66</sup>. Talonen et al. reported similar findings in austenitic steel, which showed  $\alpha'$ -martensite at the fractured surface but a progressive decrease with distance from it<sup>67</sup>. A similar trend was observed by Hossain et al. at compressive stresses in excess of 500 MPa, with the hexagonal close-packed structured  $\epsilon$ -martensite transformation observed at randomly spaced stacking faults, and nucleation of  $\alpha'$ -martensite at shear band intersections<sup>49</sup>. Zhao et al. observed blocky  $\gamma$ -austenite in high-carbon steel similar to that shown in Fig. 14b and reported its transformation to martensite after tensile loading and 5% strain<sup>68</sup>. They noted the transformation followed the Kurdjumov-Sachs relationship, induced by the lower stability of the blocky austenite and its less uniform carbon distribution. Shear bands are observed in high-resolution electron microscopy image of the work-hardened region (Fig. 14c). The intersection of these shear bands is reported as a favourable nucleation site for  $\alpha'$ -martensite, with greater nucleation reported with increasing stress, resulting in a corresponding reduction in the  $\gamma$ -austenite phase<sup>68–70</sup>. The retention of  $\gamma$ -austenite is desired in the manufacture of transformation-induced plasticity (TRIP) and twinning-induced plasticity steels, highlighted by the slightly improved mechanical performance of the banded sample by the TRIP effect as reported by He et al.<sup>70</sup>. Further reported is the preference for enlarged (>20  $\mu\text{m}$ )  $\gamma$ -austenite grains with lower carbon content for TRIP transformation due to lower mechanical stability facilitating transformation at a lower stress and strain levels. With a lower retained  $\gamma$ -austenite content due to the continual tempering of the process, the monolithic sample of Fig. 13b shows a reduction in work hardening transformation and, thus, a more brittle behaviour.

## Discussion

Manipulation of the melt pool shape through selective laser beam defocusing represents a level of microstructural control strategy, which offers finer spatial resolution, improved accuracy, and more convenience compared to what other researchers have reported in the literature<sup>11,12,71</sup>. For instance, microstructure architectures with site-specific phases using laser elemental ablation have shown spatial resolution limits dependent on melt pool size, which are a factor 2 larger than ours (200  $\times$  350  $\mu\text{m}$ ) owing to the greater energy density used (500 J/mm<sup>3</sup>)<sup>11</sup>. Furthermore, this approach is prone to phase transformation inaccuracies due to inhomogeneous element dissipation, leaving regions of mixed-phase content. Finally, the need for vastly different laser energy densities or the use of multiple re-melting laser scan passes to retain and/or ablate elements is time-consuming and inconvenient to implement using current laser control software.

While laser remelting processes have shown layerwise phase control in regions between 40 and 75  $\mu\text{m}$  in width, this process often results in discontinuous microstructures—unlike the ones we have presented here—due to thermal gradient fluctuations induced by the second remelting pass<sup>12</sup>. Moreover, these strategies yield minor differences in hardness between the banded region and the matrix (0.4 GPa) compared to our work, which may decrease the benefits associated with a hetero-structure material<sup>6</sup>.

Phase control methods that employ changes in laser beam power or scanning speed to vary the volumetric energy density have low spatial resolution and accuracy, in general, as the difference in cooling rate required to induce different phase transformations occurs across a narrow processing window. This is seen with the formation of disconnected regions induced by inter-tract tempering and the intrinsic heat treatment of the process<sup>71</sup>. By contrast, our work employs manipulation of the intrinsic heat treatment and increased retention of metastable phases due to the change from conduction to keyhole melt mode, enabling higher resolution and convenience as the laser power and speed are kept constant.

Convenience, versatility, and property (hardness) contrast are perhaps the greatest achievements of our phase control methodology. As exemplified

in the “NTU” sample presented in Fig. 2, we can “architect” the final microstructure by varying the focal offset in 3-D in a reproducible and consistent manner. This new strategy is well fit to the design paradigm of hetero-structure materials, where there is a growing interest in the development of materials with 3-D microstructural control to impart improved properties. The results in Fig. 11 are similar to the lamellar solids used in the field of hetero-structured materials, while those in Fig. 12 are comparable to rod-reinforced composites<sup>6,72</sup>. This site-specific phase control principle yields phase transformations without the requirement for element evaporation, opening opportunities to tune phase content in other alloy systems without property trade-offs. Furthermore, the focal offset could be varied in *operando*, during laser scanning, enabling phase change along the scan line plane and the production of microstructural gradients at the resolution of a scan line. We exemplified the application of this new phase control principle with the use of an in-situ high-carbon alloyed steel. However, greater mechanical property improvements could be obtained if this strategy were implemented on a different alloy system, such as maraging steels (FeNiTi, FeNiAl, 18Ni300 etc.), which have improved ductility from fine  $\gamma$ -austenite grain growth along melt pool boundaries and high strength from precipitation strengthening<sup>10,16,73–75</sup>.

The major drawback of this work is the limited plasticity of the case-study alloy—both with a monolithic as well as an architected microstructure. This is the main reason, we conclude, why we could not find evidence of hetero-deformation induced strengthening. We ascribe the alloy's brittle-like behaviour to the high carbon content, which yields a large fraction of  $\alpha'$ -martensite and thus quench-embrittlement<sup>63</sup>, even in the tempered microstructure (see Table 2). Moreover, porosity and solidification cracking are also known to contribute to brittle-like behaviour. The fact that pores or cracks may be aligned within keyhole MPB regions or along keyhole melt pool centerlines, respectively, exacerbates their negative influence on mechanical properties by creating easy preferential crack paths. To mitigate these problems, we suggest the employment of a scanning strategy that involves scan rotation of each layer with multifactorial periodicity. The 67° scan rotation strategy is a good example strategy, which was proven effective in mitigating strain accumulation too. We note, however, that employing a scan strategy with arbitrary rotation while ensuring site-specific phase control is challenging, especially when attempting to engineer complex 3-D microstructure architectures comprising both horizontal and vertical MPBs (e.g., Fig. 1)<sup>76</sup>. Should this level of control be available, we speculate that periodical rotation of scan lines would also improve the roughness of the top surface induced by keyhole MPBs, as the peak and trough formations between adjacent melt pools would be distributed randomly along the build direction<sup>77</sup>. Similar benefits could also apply to pores and solidification cracking.

With regard to the latter, we propose that minimising the temperature difference between the solidified metal and the melt pool could potentially limit cracking by decreasing the volume fraction of  $\alpha'$ -martensite. This could be achieved by pre-heating the substrate or the powder bed below the annealing and martensite starting temperature<sup>29,78,79</sup>. The drawback of this solution, however, would be a decreased property contrast. Alternatively, post-process heat treatments could be used to obtain a solid solution strengthened steel of hard and soft  $\alpha'$ -martensite regions, induced by selective partitioning of alloying elements during L-PBF<sup>80</sup>.

Besides engineering the mechanical properties, our phase control method may find potential applications when other site-specific property enhancement is needed, such as wear and corrosion resistance as well as soft magnetism. Furthermore, through the employment of a rotating scanning strategy we could create bioinspired Bouligand structures of hard and soft phases for improved toughness and fracture resistance. Indeed, producing  $\alpha'$ -martensite carbon steels by L-PBF without the need for costly post-process carburisation would be advantageous from an economic standpoint<sup>81–83</sup>. Another possible application of this phase control method is in part identification, by selectively retaining un-tempered  $\alpha'$ -martensite to create recognizable “patterns” to identify parts upon tint etchants under a simple optical microscope (e.g., Fig. 2)<sup>8,84</sup>.

## Methods

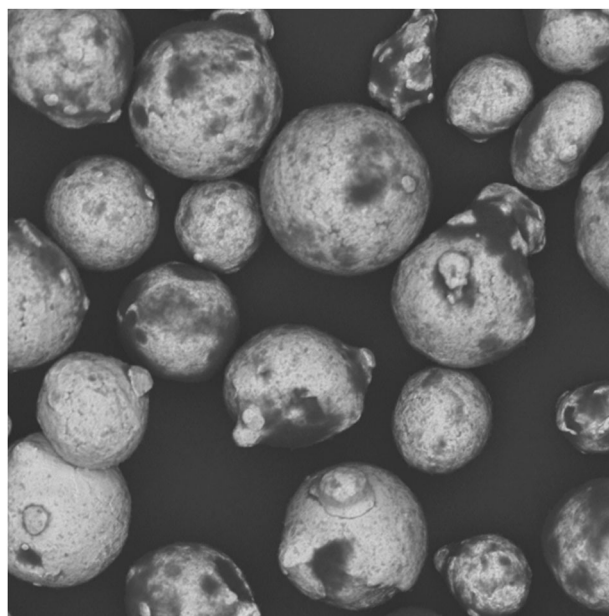
For the experiments detailed in this work, we used a mixture of gas-atomised Sandvik Osprey AISI 8620 low alloy steel powder (15–53  $\mu\text{m}$  in size) and 1 wt% Cabot 660 carbon black, which we prepared using an Inversina tumbler mixer for 8–10 hours. The distribution of carbon coating the AISI 8620 powder particles is evident in the SEM image Fig. 15, with black spots indicative of carbon. The rationale for studying a high carbon (C) steel was to push all diffusional phase transformations to longer times to ensure the retention of a super-saturated solid solution upon cooling, as well as to account for uncontrolled carbon losses during processing. To verify the alloy composition in the as-built state, we employed combustion infrared absorbance to analyse carbon and sulphur and inductively coupled plasma atomic emission spectroscopy for the remaining elements. The results for different samples produced in this study are shown in Table 3. We include the measurement uncertainty in Supplementary Table 1. Carbon loss during the printing process is evident, and it is likely the result of vaporisation because of the high energy input, or a reaction with residual oxygen in the chamber<sup>83,85</sup>. As expected, however, the final carbon content is sufficient to create a super-saturated matrix and induce a high content of martensite.

The in-house developed L-PBF machine employed an SPI G4 nano-second pulse laser, which was controlled by a Cambridge Technology ProSeries II scan head and focused using an F-theta lens. A square wave pulse waveform was employed in this work with a repetition frequency of 950 kHz, pulse on time of 261 ns and pulse peak power of 1100 W<sup>86</sup>. We manufactured  $6 \times 6 \times 6$  mm and  $8 \times 8 \times 8$  mm cubes for microstructural evaluation and  $12 \times 12 \times 38$  mm blocks for micro-tensile testing, all atop an AISI 8620 substrate. We produced samples with a laser power of 200 W, hatch spacing of 120  $\mu\text{m}$ , powder layer thickness of 50  $\mu\text{m}$ , and laser

scanning speed of 400 mm/s, which corresponded to a laser energy density of 83 J/mm<sup>3</sup>. We produced all samples using a serpentine scanning strategy over the whole surface with no rotation in between layers. We set the laser scan direction perpendicular to nitrogen gas flow and parallel to the direction of powder spreading. To control the resulting crystallographic phases we varied the laser focus within a range between 0 mm (in-focus) and +4 mm. We further tuned the sample base temperature during L-PBF by introducing dwell time delays of up to 1 min after each layer to ensure that we consistently form martensite upon solidification. Similar dwells were done in other works focused on phase control<sup>10,16,73</sup>.

We used electro-discharge machining to cut samples off the build plate into dog bone-shaped samples for tensile testing or along different cross-sections for microstructural evaluation. We estimated build density by averaging three repeated Archimedes tests using a Mettler Toledo XS204 mass balance and by immersing the samples into a bath of 99% Ethanol. We prepared the samples for microstructure analysis by hot mounting in a conductive resin, followed by grinding in diminishing grits up to a final polish with a 1  $\mu\text{m}$  diamond suspension for optical microscopy analysis and 0.25  $\mu\text{m}$  colloidal silica suspension for scanning electron microscopy (SEM). To characterize the microstructure we etched the polished sample surface with Nital reagent (containing 2% Nitric acid) for 10 s, followed by evaluation using an Olympus MX40 optical microscope at magnifications from  $\times 2.5$  to  $\times 500$ . To assess the influence of laser focal offset on melt pool morphology, we took melt pool depth measurements of cross-sectioned discrete samples produced at each focal offset (0, 1, 2, 3, and 4 mm) at 16 locations along the line scan. Each image was taken with a magnification of  $\times 100$  using the Olympus Stream imaging software with calibrated in-built measurement tools. We used a JEOL FESEM 7800 F Prime to acquire backscattered electron images as well as electron backscatter diffraction (EBSD, Oxford Instruments Symmetry S2) measurements to map the crystallographic phase distribution. EBSD measurements used an accelerating voltage of 20 kV, probe current of 20 nA, and step size of 0.15 and 0.08  $\mu\text{m}$  for low- and high-magnification maps, respectively. We analysed EBSD maps using AZTecCrystal software. Higher resolution imaging was obtained from transmission electron microscopy (TEM) with images taken from a lamella produced by a focus ion beam (FIB) on a FIB Zeiss Crossbeam 540. We carried out the TEM analysis using a JEOL-ARM300 aberration-corrected microscope at 300 kV using a cold field emission gun. We analysed the SAED using JEMS software. We collected the PED data using a Stingray camera and analyzed the measurements by means of the ASTAR system supplied by Nanomegas. The PED measurements were performed with a precession angle of  $0.28^\circ$  and a precession frequency of 100 Hz with an exposure time of 0.01 second per frame. We confirmed the presence of crystallographic phases in the bulk by means of XRD using a Bruker D8 Advance diffractometer with a CuK $\alpha$  radiation source ( $\lambda = 0.154$  nm), which we operated at 40 kV at an emission current of 40 mA. We set the XRD scanning speed to  $1^\circ/\text{min}$  across the  $2\theta$  range between  $5^\circ$  and  $90^\circ$ . We indexed the XRD patterns with the use of Match! software. We also assessed the content of ferrite in our samples by taking five measurements using a Fischer FMP30 Feritscope.

To assess the local mechanical properties of the multi-phase samples, we employed nano hardness measurements using an Agilent Technologies G200 machine equipped with a Berkovich indenter. We used continuous stiffness mode with a maximum displacement of 1000  $\mu\text{m}$ . We took indents in three sets for each sample, with starting indents proceeding below the martensite-dominated melt pool and subsequent indents taken along the



50 $\mu\text{m}$

**Fig. 15 | Powder analysis.** AISI 8620 low alloy steel powder mixed with 1 wt% Carbon, black regions on particles indicate carbon coating.

**Table 3 | Powder and sample composition in wt%**

	Fe	C	Mn	Ni	Cr	Si	Mo	P	S
Powder	Bal	1.22	0.7	0.6	0.5	0.32	0.22	0.007	0.006
Banded microstructure	Bal	0.87	0.71	0.70	0.55	0.31	0.22	<0.01	0.009
Monolithic	Bal	0.89	0.71	0.71	0.55	0.31	0.22	<0.01	0.01



build direction at 20  $\mu\text{m}$  increments in five columns spaced 50  $\mu\text{m}$  apart. Three columns were used in the architecture sample. We characterized the nano-indent by means of optical microscopy at a magnification of  $\times 100$  and  $\times 200$ .

We carried out the micro tensile tests on samples with a gage length of 8 mm, width of 2 mm, and thickness of 1 mm. We employed a strain rate of 0.008 mm/s on a Shimadzu AGS-X 50kN tensile tester utilising an optical extensometer with five repeated trials for each sample condition. We also recorded testing machine compliance using a rigid steel bar at the same sample strain rate of 0.008 mm/s to a maximum load of 2000N, which exceeds that exerted on the micro tensile samples. We then subtracted the compliance curve from the sample's tensile curves.

## Data availability

No datasets were generated or analysed during the current study.

Received: 28 October 2024; Accepted: 25 February 2025;

Published online: 30 March 2025

## References

- Li, H., Thomas, S. & Hutchinson, C. Delivering microstructural complexity to additively manufactured metals through controlled mesoscale chemical heterogeneity. *Acta Mater.* **226**, 117637 (2022).
- Gao, S. et al. Additive manufacturing of alloys with programmable microstructure and properties. *Nat. Commun.* **14**, 6752 (2023).
- Yang, G. & Kim, J.-K. Hierarchical precipitates, sequential deformation-induced phase transformation, and enhanced back stress strengthening of the micro-alloyed high entropy alloy. *Acta Mater.* **233**, 117974 (2022).
- Shi, P. et al. Hierarchical crack buffering triples ductility in eutectic herringbone high-entropy alloys. *Science* **373**, 912–918 (2021).
- Lu, K. Nanomaterials. Making strong nanomaterials ductile with gradients. *Science* **345**, 1455–1456 (2014).
- Zhu, Y. et al. Heterostructured materials: superior properties from hetero-zone interaction. *Mater. Res. Lett.* **9**, 1–31 (2020).
- Jeong, S. G. et al. Architected heterogeneous alloys with selective laser melting. *Scr. Mater.* **208**, 114332 (2022).
- Sofinowski, K., Wittwer, M. & Seita, M. Encoding data into metal alloys using laser powder bed fusion. *Addit. Manuf.* **52**, 102683 (2022).
- Gao, S., Liu, R., Huang, R., Song, X. & Seita, M. A hybrid directed energy deposition process to manipulate microstructure and properties of austenitic stainless steel. *Mater. Des.* **213**, 110360 (2022).
- Kurnsteiner, P. et al. High-strength Damascus steel by additive manufacturing. *Nature* **582**, 515–519 (2020).
- Arabi-Hashemi, A. et al. 3D magnetic patterning in additive manufacturing via site-specific in-situ alloy modification. *Appl. Mater. Today* **18**, 100512 (2020).
- Chen, X. & Qiu, C. In-situ development of a sandwich microstructure with enhanced ductility by laser reheating of a laser melted titanium alloy. *Sci. Rep.* **10**, 15870 (2020).
- Xu, W. et al. Additive manufacturing of strong and ductile Ti–6Al–4V by selective laser melting via in situ martensite decomposition. *Acta Mater.* **85**, 74–84 (2015).
- Nie, X. et al. Effect of defocusing distance on laser powder bed fusion of high strength Al–Cu–Mg–Mn alloy. *Virtual Phys. Prototyp.* **15**, 325–339 (2020).
- Montero-Sistiaga, M. L., Pourbabak, S., Van Humbeeck, J., Schryvers, D. & Vanmeensel, K. Microstructure and mechanical properties of Hastelloy X produced by HP-SLM (high power selective laser melting). *Mater. Des.* **165**, 107598 (2019).
- Tan, C. et al. Machine learning customized novel material for energy-efficient 4D printing. *Adv. Sci.* **10**, e2206607 (2023).
- Gentec-EO. Spot size and beam waist. Available from: <https://www.gentec-eo.com/laser-calculators/beam-waist-spot-size>. (2025).
- Saleh, B. E. A. & Teich, M. C. 3.1 The Gaussian Beam. In: *Fundamentals of Photonics*. John Wiley & Sons: Hoboken, NJ 07030, USA. p. 271–291 (2019).
- Xu, W. et al. Ti–6Al–4V additively manufactured by selective laser melting with superior mechanical properties. *JOM* **67**, 668–673 (2015).
- Cong, Z. H. et al. Stress and strain partitioning of ferrite and martensite during deformation. *Metall. Mater. Trans. A* **40**, 1383–1387 (2009).
- Godbole, K., Panigrahi, B. B. & Das, C. Tailoring of mechanical properties of AISI 410 martensitic stainless steel through tempering. In: *26th International Conference on Metallurgy and Materials 2017*, Web of Science: Brno, Czech Republic. p. 705–710 (2017).
- Hearn, W., Lindgren, K., Persson, J. & Hryha, E. in situ tempering of martensite during laser powder bed fusion of Fe–0.45C steel. *Materialia* **23**, 101459 (2022).
- Abdelwahed, M. et al. On the recycling of water atomized powder and the effects on properties of L-PBF processed 4130 low-alloy steel. *Materials* **15**, 336 (2022).
- Li, X. et al. Heterogeneously tempered martensitic high strength steel by selective laser melting and its micro-lattice: processing, microstructure, superior performance and mechanisms. *Mater. Design.* **178**, 107881 (2019).
- Williams, B., Clifford, D., El-Gendy, A. A. & Carpenter, E. E. solvothermal synthesis of Fe<sub>7</sub>C<sub>3</sub> and Fe<sub>3</sub>C nanostructures with phase and morphology control. *J. Appl. Phys.* **120**, 033904 (2016).
- Herbstein, F. H. & Snyman, J. A. Identification of Eckstrom-Adcock iron carbide as Fe<sub>7</sub>C<sub>3</sub>. *Inorg. Chem.* **3**, 894–896 (1964).
- Seede, R. et al. Effect of heat treatments on the microstructure and mechanical properties of an ultra-high strength martensitic steel fabricated via laser powder bed fusion additive manufacturing. *Addit. Manuf.* **47**, 102255 (2021).
- Seede, R. et al. An ultra-high strength martensitic steel fabricated using selective laser melting additive manufacturing: Densification, microstructure, and mechanical properties. *Acta Mater.* **186**, 199–214 (2020).
- Boes, J., Röttger, A., Mutke, C., Escher, C. & Theisen, W. Microstructure and mechanical properties of X65MoCrWV3-2 cold-work tool steel produced by selective laser melting. *Addit. Manuf.* **23**, 170–180 (2018).
- Kim, K.-S., Kim, Y.-K. & Lee, K.-A. Effect of repeated laser scanning on the microstructure evolution of carbon-bearing martensitic steel manufactured by laser powder bed fusion: quenching-partitioning drives carbon-stabilized austenite formation. *Addit. Manuf.* **60**, 103262 (2020).
- Dilip, J. J. S., Ram, G. D. J., Starr, T. L. & Stucker, B. Selective laser melting of HY100 steel: process parameters, microstructure and mechanical properties. *Addit. Manuf.* **13**, 49–60 (2017).
- Wang, L. et al. Effect of microstructure on corrosion behavior of high strength martensite steel—a literature review. *Int. J. Miner., Metall. Mater.* **28**, 754–773 (2021).
- Rong, Y., Lei, T., Xu, J., Huang, Y. & Wang, C. Residual stress modelling in laser welding marine steel EH36 considering a thermodynamics-based solid phase transformation. *Int. J. Mech. Sci.* **146–147**, 180–190 (2018).
- Zhang, G. et al. Simulation of temperature field and residual stress in high-power laser self-melting welding process of CLF-1 steel medium-thick plate. *Fusion Eng. Des.* **195**, 113936 (2023).
- Mirkoohi, E., Li, D., Garmestani, H. & Liang, S. Y. Analytical modeling of residual stress in laser powder bed fusion considering volume conservation in plastic deformation. *Modelling* **1**, 242–259 (2020).
- Baghdadchi, A., Hosseini, V. A. & Karlsson, L. Identification and quantification of martensite in ferritic-austenitic stainless steels and welds. *J. Mater. Res. Technol.* **15**, 3610–3621 (2021).

37. Davidson, K. P., Littlefair, G. & Singamneni, S. On the machinability of selective laser melted duplex stainless steels. *Mater. Manuf. Process.* **37**, 1–17 (2021).
38. Sofinowski, K. A., Raman, S., Wang, X., Gaskey, B. & Seita, M. Layer-wise engineering of grain orientation (LEGO) in laser powder bed fusion of stainless steel 316L. *Addit. Manuf.* **38**, 101809 (2021).
39. Garibaldi, M., Ashcroft, I., Simonelli, M. & Hague, R. Metallurgy of high-silicon steel parts produced using Selective Laser Melting. *Acta Mater.* **110**, 207–216 (2016).
40. Zhao, Z. et al. Texture dependence on the mechanical properties of 18Ni300 maraging steel fabricated by laser powder bed fusion. *Mater. Charact.* **189**, 111938 (2022).
41. Binkley, M. Microstructure development in multi-pass laser melting of AISI 8620 steel. In: School of Materials Engineering. Purdue University: Purdue University (2020).
42. Liu, F. et al. Effect of tempering temperature on microstructure and mechanical properties of laser solid formed 300M steel. *J. Alloy. Compd.* **689**, 225–232 (2016).
43. Hocine, S. et al. A miniaturized selective laser melting device for operando X-ray diffraction studies. *Addit. Manuf.* **34**, 101194 (2020).
44. Bhadeshia, H. K. D. H. Bainite in steels - transformations, microstructure and properties. 2 edn. Cambridge, UK: The University Press (2001).
45. Talebi, S. H., Jahazi, M. & Melkonyan, H. Retained austenite decomposition and carbide precipitation during isothermal tempering of a medium-carbon low-alloy bainitic steel. *Materials* (Basel). **11**, 1441 (2018).
46. Yan, G., Han, L., Li, C., Luo, X. & Gu, J. Characteristic of retained austenite decomposition during tempering and its effect on impact toughness in SA508 Gr.3 steel. *J. Nucl. Mater.* **483**, 167–175 (2017).
47. Bhadeshia, H. K. D. H. Theory and significance of retained austenite in steels. University of Cambridge. p. 127 (1980).
48. Mola, J. & Ren, M. On the hardness of high carbon ferrous martensite. *IOP Conf. Ser.: Mater. Sci. Eng.* **373**, 012004 (2018).
49. Hossain, R., Pahlevani, F., Quadir, M. Z. & Sahajwalla, V. Stability of retained austenite in high carbon steel under compressive stress: an investigation from macro to nano scale. *Sci. Rep.* **6**, 34958 (2016).
50. Wei, K. et al. Mechanical properties of Invar 36 alloy additively manufactured by selective laser melting. *Mater. Sci. Eng. A*. **772**, 138799 (2020).
51. Shrestha, S. & Chou, K. Residual heat effect on the melt pool geometry during the laser powder bed fusion process. *J. Manuf. Mater. Process.* **6**, 153 (2022).
52. Patel, S. & Vlasea, M. Melting modes in laser powder bed fusion. *Materialia* **9**, 100591 (2020).
53. Khorasani, M. et al. A comprehensive study on meltpool depth in laser-based powder bed fusion of Inconel 718. *Int. J. Adv. Manuf. Technol.* **120**, 2345–2362 (2022).
54. Phua, A., Cook, P. S., Davies, C. H. J. & Delaney, G. W. Powder spreading over realistic laser melted surfaces in metal additive manufacturing. *Addit. Manuf. Lett.* **3**, 100039 (2022).
55. Lu, Q., Grasso, M. Le, T.-P. & Seita, M. Predicting build density in L-PBF through in-situ analysis of surface topography using powder bed scanner technology. *Addit. Manuf.* **51**, 102626 (2022).
56. Le, T.-P., Wang, X., Davidson, K. P., Fronda, J. E. & Seita, M. Experimental analysis of powder layer quality as a function of feedstock and recoating strategies. *Addit. Manuf.* **39**, 101890 (2021).
57. Kou, S. *Welding Metallurgy*. 2 edn, John Wiley & Sons, Inc (2002).
58. Wei, H. L., Elmer, J. W. & DebRoy, T. Crystal growth during keyhole mode laser welding. *Acta Mater.* **133**, 10–20 (2017).
59. Kadoi, K., Fujinaga, A., Yamamoto, M. & Shinozaki, K. The effect of welding conditions on solidification cracking susceptibility of type 310S stainless steel during laser welding using an in-situ observation technique. *Welding in the World*, (2013).
60. Huitron, R. M. P. & Vuorinen, E. Hot cracking of structural steel during laser welding. *IOP Conf. Ser.: Mater. Sci. Eng.* **258**, 012005 (2017).
61. Sun, L. et al. A novel ultra-high strength maraging steel with balanced ductility and creep resistance achieved by nanoscale  $\beta$ -NiAl and Laves phase precipitates. *Acta Mater.* **149**, 285–301 (2018).
62. Das, D. & Chattopadhyay, P. P. Influence of martensite morphology on the work-hardening behavior of high strength ferrite–martensite dual-phase steel. *J. Mater. Sci.* **44**, 2957–2965 (2009).
63. Krauss, G. Deformation and fracture in martensitic carbon steels tempered at low temperatures. *Metall. Mater. Trans. B* **32**, 205–221 (2001).
64. Yang, D. & Xiong, Z. Fracture behavior of a one-step quenching and partitioning steel characterised using uniaxial tension and double edge-notched tension. *J. Phys. Conf. Ser.* **1653**, 012023 (2020).
65. Banerjee, A., Gangadhara Prusty, B., Zhu, Q., Pahlevani, F. & Sahajwalla, V. Strain-rate-dependent deformation behavior of high-carbon steel under tensile–compressive loading. *Jom* **71**, 2757–2769 (2019).
66. Polatidis, E. et al. Suppressed martensitic transformation under biaxial loading in low stacking fault energy metastable austenitic steels. *Scr. Mater.* **147**, 27–32 (2018).
67. Talonen, J., Nenonen, P., Pape, G. & Hänninen, H. Effect of strain rate on the strain-induced  $\gamma$ - $\alpha'$ -martensite transformation and mechanical properties of austenitic stainless steels. *Metall. Mater. Trans. A* **36A**, 421–432 (2005).
68. Zhao, F. et al. Martensite transformation of retained austenite with diverse stability and strain partitioning during tensile deformation of a carbide-free Bainitic steel. *Mater. Charact.* **179**, 111327 (2021).
69. Talonen, J. & Hänninen, H. Formation of shear bands and strain-induced martensite during plastic deformation of metastable austenitic stainless steels. *Acta Mater.* **55**, 6108–6118 (2007).
70. He, B. B., Luo, H. W. & Huang, M. X. Experimental investigation on a novel medium Mn steel combining transformation-induced plasticity and twinning-induced plasticity effects. *Int. J. Plast.* **78**, 173–186 (2016).
71. Kim, D., Ferretto, I., Jeon, J. B., Leinenbach, C. & Lee, W. Formation of metastable bcc- $\delta$  phase and its transformation to fcc- $\gamma$  in laser powder bed fusion of Fe–Mn–Si shape memory alloy. *J. Mater. Res. Technol.* **14**, 2782–2788 (2021).
72. Shao, C. et al. Architecture of high-strength aluminum–matrix composites processed by a novel microcasting technique. *NPG Asia Mater.* **11**, 69 (2019).
73. Amirabdollahian, S. et al. Towards controlling intrinsic heat treatment of maraging steel during laser directed energy deposition. *Scr. Mater.* **201**, 113973 (2021).
74. Takata, N., Nishida, R., Suzuki, A., Kobashi, M. & Kato, M. Crystallographic features of microstructure in maraging steel fabricated by selective laser melting. *Metals* **8**, 440 (2018).
75. Kürnsteiner, P. et al. Massive nanoprecipitation in an Fe–19Ni–xAl maraging steel triggered by the intrinsic heat treatment during laser metal deposition. *Acta Mater.* **129**, 52–60 (2017).
76. Qin, S. et al. Influence of process parameters on porosity and hot cracking of AISI H13 fabricated by laser powder bed fusion. *Powders* **1**, 184–193 (2022).
77. Robinson, J. H., Ashton, I. R. T., Jones, E., Fox, P. & Sutcliffe, C. The effect of hatch angle rotation on parts manufactured using selective laser melting. *Prototyp. J.* **25**, 289–298 (2019).
78. Köhler, M. L. et al. Influence of Cr3C2 additions to AISI H13 tool steel in the LPBF process. *Steel Res. Int.* **93**, 2100454 (2021).
79. Moradiani, A., Ghaini, F. M., Beiranvand, Z. M., Chandima Ratnayake, R. M. & Aliabadi, A. Effect of laser pulse power on solidification cracking susceptibility in surface processing of a high carbon high chromium tool steel. *CIRP J. Manuf. Sci. Technol.* **38**, 737–747 (2022).
80. Kim, J. H. et al. Microstructure and tensile properties of chemically heterogeneous steel consisting of martensite and austenite. *Acta Mater.* **223**, 117506 (2022).

81. Sari, U., Kırındı, T., Yüksel, M. & Ağan, S. Influence of Mo and Co on the magnetic properties and martensitic transformation characteristics of a Fe-Mn alloy. *J. Alloy. Compd.* **476**, 160–163 (2009).
82. Pantelis, D. I., Bouyiouri, E., Kouloumbi, N., Vassiliou, P. & Koutsomichalis, A. Wear and corrosion resistance of laser surface hardened structural steel. *Surf. Coat. Technol.* **298**, 125–134 (2002).
83. Schmitt, M. et al. Carbon particle in-situ alloying of the case-hardening steel 16MnCr5 in laser powder bed fusion. *Metals* **11**, 896 (2021).
84. Plotkowski, A. et al. A stochastic scan strategy for grain structure control in complex geometries using electron beam powder bed fusion. *Addit. Manuf.* **46**, 102092 (2021).
85. Zhao, X. et al. Decarburization of stainless steel during selective laser melting and its influence on Young's modulus, hardness and tensile strength. *Mater. Sci. Eng.: A* **647**, 58–61 (2015).
86. Demir, A. G., Mazzoleni, L., Caprio, L., Pacher, M. & Previtali, B. Complementary use of pulsed and continuous wave emission modes to stabilize melt pool geometry in laser powder bed fusion. *Opt. Laser Technol.* **113**, 15–26 (2019).

## Acknowledgements

We Acknowledge Alpravinosh Alagesan for image processing, Raman Sudharshan for contributing to the project conceptualisation, Poh Zhen Yang Andre and Lim Han Siang Winston for helping with sample preparation, Xiaogang Wang for suggesting a baseline process parameter selection, Alan Lim for supporting with EBSD characterisation, Chris Boothroyd for carrying out TEM measurements. The authors acknowledge the Facilities for Analysis, Characterization, Testing and Simulations (FACTS) at NTU for access to electron microscopy equipment.

## Author contributions

K.P.D.—conceptualization, methodology, writing original draft, writing review and editing, investigation, validation, formal analysis, visualisation, data curation. T.P.L.—writing review and editing, data curation, formal analysis, visualisation. L.L.N.—investigation, data curation, formal analysis. J.E.P.F., R.L., T.L.M., and Y.Y.T.—investigation. M.S.—methodology, writing

original draft, writing review and editing, resources, supervision, project administration, funding acquisition.

## Competing interests

The authors declare no competing interests.

## Additional information

**Supplementary information** The online version contains supplementary material available at <https://doi.org/10.1038/s44334-025-00022-3>.

**Correspondence** and requests for materials should be addressed to Matteo Seita.

**Reprints and permissions information** is available at <http://www.nature.com/reprints>

**Publisher's note** Springer Nature remains neutral with regard to jurisdictional claims in published maps and institutional affiliations.

**Open Access** This article is licensed under a Creative Commons Attribution-NonCommercial-NoDerivatives 4.0 International License, which permits any non-commercial use, sharing, distribution and reproduction in any medium or format, as long as you give appropriate credit to the original author(s) and the source, provide a link to the Creative Commons licence, and indicate if you modified the licensed material. You do not have permission under this licence to share adapted material derived from this article or parts of it. The images or other third party material in this article are included in the article's Creative Commons licence, unless indicated otherwise in a credit line to the material. If material is not included in the article's Creative Commons licence and your intended use is not permitted by statutory regulation or exceeds the permitted use, you will need to obtain permission directly from the copyright holder. To view a copy of this licence, visit <http://creativecommons.org/licenses/by-nc-nd/4.0/>.

© The Author(s) 2025